

Suparno Bhattacharyya

Department of Engineering
Science and Mechanics,
Pennsylvania State University,
University Park, PA 16802
e-mail: sxb1086@psu.edu

Joseph P. Cusumano¹

Department of Engineering
Science and Mechanics,
Pennsylvania State University,
University Park, PA 16802
e-mail: jpc3@psu.edu

An Energy Closure Criterion for Model Reduction of a Kicked Euler–Bernoulli Beam

Reduced order models (ROMs) can be simulated with lower computational cost while being more amenable to theoretical analysis. Here, we examine the performance of the proper orthogonal decomposition (POD), a data-driven model reduction technique. We show that the accuracy of ROMs obtained using POD depends on the type of data used and, more crucially, on the criterion used to select the number of proper orthogonal modes (POMs) used for the model. Simulations of a simply supported Euler–Bernoulli beam subjected to periodic impulsive loads are used to generate ROMs via POD, which are then simulated for comparison with the full system. We assess the accuracy of ROMs obtained using steady-state displacement, velocity, and strain fields, tuning the spatiotemporal localization of applied impulses to control the number of excited modes in, and hence the dimensionality of, the system's response. We show that conventional variance-based mode selection leads to inaccurate models for sufficiently impulsive loading and that this poor performance is explained by the energy imbalance on the reduced subspace. Specifically, the subspace of POMs capturing a fixed amount (say, 99.9%) of the total variance underestimates the energy input and dissipated in the ROM, yielding inaccurate reduced-order simulations. This problem becomes more acute as the loading becomes more spatio-temporally localized (more impulsive). Thus, energy closure analysis provides an improved method for generating ROMs with energetics that properly reflect that of the full system, resulting in simulations that accurately represent the system's true behavior.

[DOI: 10.1115/1.4048663]

Keywords: model order reduction, proper orthogonal decomposition (POD), reduced order model (ROM), dynamical systems, modal analysis, energy closure analysis, energy balance, structural vibration

Introduction

Analyzing and understanding the behavior of any high-dimensional system is greatly facilitated if one can find a simpler model that nevertheless well-describes its behavior. Simulations of high-dimension models are often computationally heavy and generate large volumes of data that can significantly hinder analysis. However, the *effective* dimensionality of such systems is often significantly lower than the fundamental dimensionality obtained from their first-principles formulation. The estimation of a system's effective dimension is thus of primary importance when attempting to formulate a much lower-dimensional model that can accurately approximate a behavior of interest.

In this work, we study the performance of the proper orthogonal decomposition (POD) when used for model reduction of a high-dimensional system undergoing structural vibrations. The proper orthogonal decomposition is a statistical tool that can be used to obtain a low-dimensional approximation of high-dimensional data by identifying and capturing its dominant features. This is achieved through a variance-based decomposition of the data that leads to a relatively small number of empirical shape functions known as proper orthogonal modes (POMs). The POMs maximize the amount of data variance captured per mode and, thus, POD provides a low dimensional representation of the original data that is optimal in the least-squares sense.

POD has a broad spectrum of applications across multiple disciplines. It is widely used for studying the structure of low-dimensional dynamics in fluid systems [1–3]. POD is also used extensively in wind and ocean engineering applications, and in

the atmospheric sciences, where the POMs are referred to as empirical orthogonal functions (EOFs) [4–9]. Other application areas of POD include linear and nonlinear control systems [10,11], acoustics [12], neuroscience [13–15], and optical systems [16]. In Refs. [17,18], POD was first used in the context of structural dynamics to characterize spatial coherence and estimate the effective dimensionality of different types of flexible nonlinear oscillators. Feeny et al. in Refs. [19,20] studied how POMs obtained using POD are related to the linear normal modes of structural systems.

However, POD, while an effective tool for *data* reduction, was never aimed at performing *model* order reduction. Still, it has been widely used for this purpose in a number of works [21–31]. POD has been implemented using data from displacement fields [21–27], as well as both displacement and velocity fields [28–31]. In Ref. [32], a theoretical upper bound for the modeling error is obtained, showing that it is proportional to the two-norm of the data projection error. However, such an analytical bound, while useful, provides no physical insight into the conditions necessary for model accuracy.

The accuracy of reduced order models (ROMs) is limited primarily by the process used to estimate the effective dimensionality of the system. Given that POD is based on the analysis of a data set's covariance structure, the associated low-dimensional subspace has been typically selected so that it captures a predefined percentage (typically more than 99% [1,2]) of the total data variance. However, while performing model reduction, the governing differential equations of a system are projected onto the same subspace estimated via POD for data reduction. Unfortunately, the optimality of POD when used for data reduction is not guaranteed to be similarly optimal when used to obtain ROMs. ROMs formulated in this manner may thus fail to capture important dynamical features of the original system, especially those with small variances [33].

For this reason, in POD-based model reduction, the dimension of the ROM is generally chosen by trial and error, until one is found that results in low modeling error. One frequently finds that the

¹Corresponding author.

Contributed by the Design Engineering Division of ASME for publication in the JOURNAL OF VIBRATION AND ACOUSTICS. Manuscript received June 4, 2020; final manuscript received September 22, 2020; published online November 2, 2020. Assoc. Editor: Shahrzad Towfighian.

fraction of total variance needed can vary significantly, not only between systems but also between different dynamical responses of the same system. For some systems, a subspace that captures 99% of the total variance of the data yields sufficiently accurate ROMs, whereas in other systems subspaces that capture 99.9% [22] or 99.99% [26] of the total variance are needed. As one example, the convergence of ROMs for the 39-story Pirelli Tower in Milan, Italy was studied in Ref. [27]. It was found that a four degrees-of-freedom (four POM) model that captures 99.99% of the total variance of the input data was far more accurate than a one-dimensional model capturing 99% of the variance. To date, there has been no physical explanation proposed for why the accuracy of ROMs obtained in such situations changes with the percentage of the variance captured by the reduced subspace furnished by POD.

In Refs. [33–36], an approach was proposed for selecting the dimension of ROMs using the concept of “dynamical consistency.” This approach takes into account the state-space dynamics of the system generating the data, but it is fundamentally tied to the study of chaotic steady-states, for which delay reconstruction can be applied. In this paper, we propose an alternative, energy-based approach for estimating the dimension of POD-based ROMs. Guo and Przekop in Ref. [37] proposed an energy-based mode selection approach where individual POMs with a major contribution to the total energy of the full order system (FOS) were selected to formulate ROMs. We, however, show that the fraction of variability needed for POD to yield an accurate ROM is explained by an examination of the energy *balance* on the reduced subspace.

For this work, we studied a periodically “kicked” simply supported Euler–Bernoulli beam undergoing steady-state oscillations. This system was chosen because impulsive loads generally excite a large number of modes. We controlled the “impulsivity” of the load by tuning its spatiotemporal localization, thereby controlling the number of excited modes in the system’s response, and hence its effective dimensionality. We simulated the system with varying degrees of impulsivity, and in each case generated displacement, velocity, and strain data to use for model reduction. For each case, we formulated a ROM and assessed its modeling error.

More importantly, however, we studied the accuracy of ROMs generated using the conventional variance-based mode selection criterion. We show that this approach yields inaccurate models for sufficiently impulsive loading conditions and that its poor performance is explained by the energy imbalance on the reduced subspace. Specifically, the energy input and dissipated in the system can be substantially underestimated on the associated reduced subspace, even when it optimally captures a fixed percentage of the data variance. Furthermore, this problem becomes more acute as the loading becomes more “impulsive” (i.e., more spatiotemporally localized). By replacing the variance-based selection criterion with one based on energy balance, we are able to reliably identify the proper effective dimension of the system. ROMs formulated on such energetically closed subspaces are found to represent the system’s true behavior with significant accuracy.

Portions of this work have previously appeared, in abbreviated form, in a conference paper by the authors [38].

Dynamics of the Kicked Beam

We consider an Euler–Bernoulli beam, simply supported at both ends and subjected to a periodic “impulsive” loading condition. Dissipation in the beam is modeled as Rayleigh damping. The displacement of the beam, as measured from the neutral axis, is represented by the scalar variable $w(x, t)$. The dimensionless equation of motion of the system is [39]

$$w''''(x, t) + c_v \dot{w}(x, t) + c_m \ddot{w}(x, t) + \ddot{w}(x, t) = F(x, t) \quad (1a)$$

with boundary conditions

$$\begin{aligned} w(0, t) = 0, \quad w''(0, t) + c_m \dot{w}''(0, t) = 0, \quad w(1, t) = 0, \\ w''(1, t) + c_m \dot{w}''(1, t) = 0 \end{aligned} \quad (1b)$$

in which: $0 \leq x \leq 1$; primes and overdots denote spatial and temporal derivatives, respectively; c_v and c_m are the coefficients of viscous and material damping, respectively. The forcing term is given by

$$F(x, t) = f(x; \epsilon, s)g(t; \tau, T) \quad (2)$$

where the spatial factor f is written as

$$f(x; \epsilon, s) = \begin{cases} \frac{2}{\epsilon} \cos^2\left(\frac{\pi}{\epsilon}(x - s)\right) & \text{for } s - \frac{\epsilon}{2} \leq x \leq s + \frac{\epsilon}{2} \\ 0 & \text{otherwise} \end{cases} \quad (3)$$

and the periodic temporal factor $g(t; \tau, T)$ is the Fourier series corresponding to the following periodic function (with period T):

$$G(t; \tau, T) = \begin{cases} \frac{2}{\tau} \cos^2\left(\frac{\pi}{\tau}(t - \frac{T}{2})\right) & \text{for } \frac{T}{2} - \frac{\tau}{2} \leq t \leq \frac{T}{2} + \frac{\tau}{2} \\ 0 & \text{otherwise} \end{cases} \quad (4)$$

in which the parameter s denotes the location on the beam where f is maximum (for this paper $s = 1/\sqrt{2}$), and T indicates the time between kicks. The parameters $\epsilon \in [0, 2(1 - s)]$ and $\tau \in [0, T]$ control the degree of “impulsivity” of the load: smaller values of ϵ and τ signify greater spatial and temporal localization, respectively. Finally, the Fourier series g (Eq. (2)) of G (Eq. (4)) is given by

$$g(t; \tau, T) = \frac{1}{T} + \sum_{k=1}^{\infty} d_k \cos\left(\frac{2\pi kt}{T}\right) \quad (5a)$$

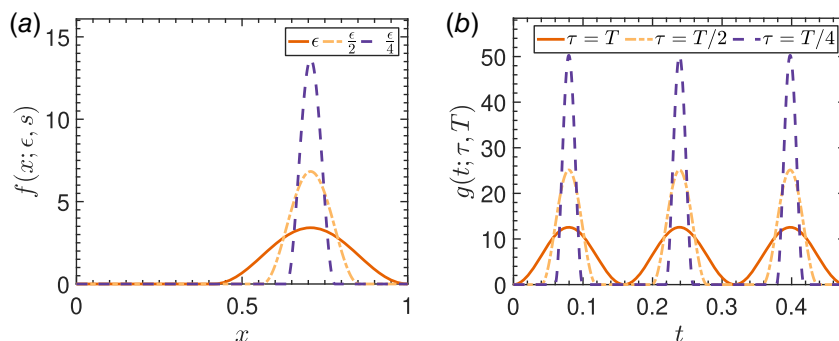


Fig. 1 The spatial and temporal factors of the forcing function (Eq. (2)). (a) Spatial factor for different values of ϵ . Function f is maximum at $s = 1/\sqrt{2}$. Here, $\epsilon = 2 - \sqrt{2}$. (b) The temporal factor g for different values of the parameter τ , which controls the duration of the “kick.” Here, time between impulses is $T = 1/2\pi$.

where

$$d_k = \begin{cases} \frac{(-1)^k}{T} & \text{for } T = k\tau \\ \frac{2(T^3 \cos(\pi k) \sin(\frac{\pi k \tau}{T}))}{T(\pi k \tau T^2 - \pi k^3 \tau^3)} & \text{otherwise.} \end{cases} \quad (5b)$$

The force density $F(x, t)$ of Eq. (2) was designed to generate a unit impulse over one forcing period, for all values of ϵ and τ , so

$$\int_0^1 \int_0^T F(x, t) dx dt = 1 \quad (6)$$

The effect of varying these parameters is illustrated in Fig. 1. We observe that as ϵ and τ decrease, the localization of the spatial and temporal factors of F increases. The peak values of these factors also increase, so that the applied forces approach the form of a delta function as ϵ and τ approach zero. This, in turn, controls the number of excited modes in, and hence the dimensionality of, the system's response.

We used symbolic algebra to determine the closed-form steady-state solution of Eq. (1a), starting with the expansion of the displacement in terms of normal modes

$$w(x, t) = \sum_{i=1}^{\infty} a_i(t) \phi_i(x) \quad (7)$$

where $\phi_k(x) = \sqrt{2} \sin(k\pi x)$ denotes the k th linear normal mode of the beam. Substitution of this expansion into Eq. (1a), together with the orthonormality of the normal modes, gives a set of decoupled ODEs in the amplitudes:

$$\ddot{a}_i + c_i \dot{a}_i + \omega_i^2 a_i = g \int_0^1 f \phi_i dx \quad (8)$$

where ω_i is the i th natural frequency of the beam, the modal damping coefficient is $c_i = c_v + c_m \omega_i^2$, and the integral on the right-hand side is

$$\int_0^1 f \phi_i dx \triangleq f_i = \begin{cases} \frac{1}{\sqrt{2}} \sin(is\pi) & \text{if } ie = 2 \\ \frac{8\sqrt{2} \sin(is\pi) \sin(\frac{ie\pi}{2})}{(4\pi ie - i^3 \epsilon^3 \pi)} & \text{otherwise.} \end{cases} \quad (9)$$

Closed-form steady-state solutions of Eq. (8) are obtained using the method of undetermined coefficients:

$$a_i = \frac{f_i}{\omega_i^2 T} + \sum_{k=1}^{\infty} (C_{ik} \cos(k\omega t) + D_{ik} \sin(k\omega t)) \quad (10a)$$

with

$$C_{ik} = \frac{d_k \alpha_k f_i}{(kc_i \omega)^2 + \alpha_k^2} \quad \text{and} \quad D_{ik} = \frac{kd_k \omega c_i f_i}{(kc_i \omega)^2 + \alpha_k^2} \quad (10b)$$

where $\omega = 2\pi/T$ is the forcing frequency, $\alpha_k = (\omega_i^2 - (k\omega)^2)$ and d_k is as in Eq. (5b).

These analytical solutions, along with the expansion in Eq. (7), were used to generate the data used to perform model reduction, as discussed in the next section. An advantage of this “semi-analytical” approach to generating the data is that it gives us direct access to the normal modes active in any given solution, providing a check on, and helping us to interpret, the proper orthogonal modes.

Variance-Based Model Reduction

Model reduction using POD is generally performed in two stages. In the first stage, a set of mutually orthogonal basis functions (known as proper orthogonal modes or POMs) is determined by the application of POD to experimental or simulation data. Then, depending on some mode selection criterion, a number of

“important” basis functions is chosen from the set to form a subspace of reduced dimension. In the next stage, the governing equations that define the full system are projected (via Galerkin projection) onto this subspace. This leads to a lower-dimensional, ROM defined by a relatively small number of coupled ordinary differential equations (ODEs) that, in principle, mimics the dynamics of the full system. A detailed description of the method is available in multiple journal articles and books (see e.g., Refs. [1,3,22,40–43]). In this section, we briefly address both of these stages of model reduction to a level of generality adequate for the scope of this paper. Then, we discuss the model reduction of the periodically kicked EB beam using the variance-based mode selection criterion.

Let $w(x, t)$ be the statistically stationary, steady-state solution of an infinite dimensional dynamical system with one spatial dimension. We assume, without loss of generality, that the temporal mean of $w(x, t)$, denoted by angle brackets $\langle w(x, t) \rangle$, is zero for each x . The solution $w \in L^2(\Omega)$, where $L^2(\Omega)$ is the Hilbert space endowed with the following inner product:

$$(w, v) = \int_{\Omega} w(x)v(x) dx \quad (11)$$

in which Ω is the spatial domain which, for the dimensionless system studied here, is given by $\Omega = [0, 1]$. Equation (11) yields an induced norm $\|w\| = \sqrt{(w, w)}$.

We wish to determine a set of functions $\psi_i(x)$ that maximize the time-averaged projection of w onto ψ , and thus minimize the associated projection error [3]:

$$\min_{\psi_i \in L^2(\Omega)} \left\langle \left\| w(x, t) - \sum_{i=1}^P (w(x, t), \psi_i) \psi_i \right\|^2 \right\rangle \quad (12)$$

in which the angle brackets $\langle \cdot \rangle$ denote the time averaging operation, and the objective function is subjected to the normality constraint $\|\psi\| = 1$. It can be shown [3] that the above minimization problem is equivalent to the following infinite-dimensional eigenvalue problem:

$$\int_{\Omega} r(x, y) \psi(y) dy = \lambda \psi(x) \quad (13)$$

where the integral kernel $r(x, y)$ is the spatial correlation function (or covariance) relating the behavior at two points $x, y \in \Omega$. That is,

$$r(x, y) = \langle w(x, t) w(y, t) \rangle \quad (14)$$

Solving the eigenvalue problem Eq. (13) leads to an infinite set of eigenfunctions $\{\psi_i\}_{i=1}^{\infty}$, which are the POMs, each with a corresponding eigenvalue λ_i that denotes the variance of $w(x, t)$ along $\psi_i(x)$. The question is then how to best select a finite number P of the ψ_i from this set to approximate $w(x, t)$.

For variance-based mode selection, one uses

$$P = \underset{p}{\operatorname{argmin}} \left\{ \mathfrak{Z}(P) : \mathfrak{Z}(P) \geq \frac{p}{100} \right\} \quad (15a)$$

where

$$\mathfrak{Z}(P) = \frac{\sum_{i=1}^P \lambda_i}{\sum_{i=1}^{\infty} \lambda_i} \quad (15b)$$

This criterion selects the smallest P (the dimension of the reduced subspace), for which the POMs capture a predefined percentage p of the total variance, $\sum_{i=1}^{\infty} \lambda_i = \langle (w, w) \rangle$. For the analyses in this paper, we selected $p = 99.9\%$. The corresponding projection error is [3,43] given by

$$\tilde{\epsilon} = \left(\sum_{j=P+1}^{\infty} \lambda_j \right)^{\frac{1}{2}} \quad (16)$$

However, the data projection error $\tilde{\epsilon}$ is *not* equivalent to the modeling error associated with the ROM. Rather, $\tilde{\epsilon}$ is simply the L^2 norm of the difference between $w(x, t)$ and its projection onto the

P dimensional subspace. In contrast, the modeling error can only be estimated once the solution of the ROM is compared with the solution of the FOS. Thus, low projection error does not imply low modeling error. The current study is motivated by this central issue.

For numerical simulations, we included $N = 100$ normal modes in the expansion Eq. (7). Thus, the steady-state displacement field for our EB beam model was expressed as

$$w(x, t) = \sum_{i=1}^N a_i(t) \phi_i(x) \quad (17)$$

In this case, the amplitudes $a_i(t)$ are known analytically (via Eqs. (10)) as are the normal modes $\phi_i(x)$, so the only errors in our generated data arise from modal truncation error (because $N < \infty$), and finite precision arithmetic. We therefore considered this 100-dimensional approximation to represent the “exact” solution to the full system.

We then determined the POMs using the displacement (w), velocity (\dot{w}), and “strain” (w') field data. The set of linear normal modes, used as the basis in Eq. (17), satisfies all boundary conditions and appropriate side conditions (e.g., differentiability) and therefore can be used to generate other admissible bases through linear transformation. We therefore express the POMs, which are yet to be found and also form a distinct admissible orthonormal basis, as a linear combination of the normal modes [1,40]:

$$\psi(x) = \sum_{j=1}^N q_j \phi_j(x) \quad (18)$$

Substituting this finite dimensional representation of $\psi(x)$ into Eq. (13) and that of $w(x, t)$ (Eq. (17)) into Eq. (14), converts the infinite-dimensional eigenvalue problem Eq. (13) into the matrix eigenvalue problem

$$\mathbf{A}\mathbf{q} = \lambda\mathbf{q} \quad (19a)$$

where $\mathbf{A} \in \mathbb{R}^{N \times N}$ is the modal correlation matrix with elements

$$A_{ij} = \langle a_i(t) a_j(t) \rangle = \frac{1}{T} \int_0^T a_i(t) a_j(t) dt \quad (19b)$$

in which we express the time average as an integral over a single forcing period, since the steady-state response is periodic. Thus, the components of the discrete eigenvectors \mathbf{q} denote coordinates, with respect to the normal modes, of a given POM $\psi(x)$.

For standard variance-based mode selection, we select a set of P eigenvectors corresponding to the P largest eigenvalues of \mathbf{A} such that the corresponding reduced subspace captures 99.9% of the total variance of the data. We anticipate that $P \ll N$. Once the subspace is defined, in the second stage of the model reduction, the equation of motion Eq. (1a) is projected onto this subspace to obtain the ROM.

To construct the reduced-order model, we expand the solution to the system with respect to the POMs:

$$w(x, t) \approx \hat{w}(x, t) = \sum_{j=1}^P b_j(t) \psi_j(x) \quad (20)$$

Substituting $\hat{w}(x, t)$ in the governing equations (1a) and employing the boundary conditions (Eq. (1b)), we obtain a system of linear second-order ODEs in terms of the proper orthogonal coordinates $b_j(t)$:

$$\ddot{\mathbf{b}} + \mathbf{C}\dot{\mathbf{b}} + \mathbf{K}\mathbf{b} = \hat{\mathbf{f}} \quad (21)$$

where the $P \times P$ stiffness matrix \mathbf{K} and $P \times 1$ reduced forcing vector $\hat{\mathbf{f}}$ have elements

$$K_{ij} = \int_0^1 \psi_i''(x) \psi_j''(x) dx \quad \text{and} \quad (22a)$$

$$\hat{f}_i = g \int_0^1 f \psi_i(x) dx \quad (22b)$$

respectively, and where f and g are as in Eq. (2). Note that in this case the mass matrix of Eq. (21) is simply the identity because the ψ_i were expressed as a linear combination of the system's mass-normalized normal modes (Eq. (18)), which are themselves orthonormal. Similarly, the damping matrix is found to be $\mathbf{C} = c_v \mathbf{I} + c_m \mathbf{K}$.

Using the eigenvectors of the stiffness matrix \mathbf{K} (symmetric, positive definite), the ROM was diagonalized and symbolic algebra was again used to determine the steady-state solutions analytically, via the method of undetermined coefficients. The displacement and velocity fields of the ROMs were then estimated using the expansion Eq. (20). Subsequently, we calculated the mean-square-error between these quantities estimated from the ROM and their exact values (Eq. (17)) and used these errors to characterize the performance of the ROM.

Accuracy of Variance-Based Reduced Order Models

While performing simulations, we used a variety of different parameter values in our model and generated three different steady-state fields: displacement, velocity, and strain. In each simulation, 90 Fourier terms were used to model the periodic temporal factor of the forcing function. Also, both resonant and nonresonant forcing frequencies were used. Furthermore, the simulations were performed with two different damping conditions: in one, the beam was subjected to only material damping; in the other, to only viscous damping. For model reduction, we selected the number P of POMs such that the associated reduced subspace captured $p = 99.9\%$ of the total data-variance. We adjusted the parameters τ and ϵ to vary the impulsivity of the forcing and thereby controlled the dimensionality of the system's response.

For a given set of parameters, displacement, velocity, and strain fields were collected from each simulation and used to formulate three different ROMs following the steps outlined in the previous section. ROMs based on the displacement field used POMs obtained using the modal covariance matrix \mathbf{A} (Eq. (19a)) with elements A_{ij} as shown in Eq. (19b). However, for ROMs using velocity field data, the relevant spatial covariance kernel (Eqs. (13) and (14)) changes to

$$r(x, y) = \langle \dot{w}(x, t) \dot{w}(y, t) \rangle \quad (23a)$$

so the elements of \mathbf{A} become

$$A_{ij} = \frac{1}{T} \int_0^T \dot{a}_i(t) \dot{a}_j(t) dt \quad (23b)$$

Similarly, for ROMs based on strain field data the appropriate covariance kernel is

$$r(x, y) = \langle w''(x, t) w''(y, t) \rangle \quad (24a)$$

and the elements of \mathbf{A} become

$$A_{ij} = \frac{\omega_i \omega_j}{T} \int_0^T a_i(t) a_j(t) dt \quad (24b)$$

where ω_i and ω_j are the i th and j th natural frequencies. For ROMs using strain data, the set of POMs was also integrated twice and orthonormalized (using the Gram-Schmidt procedure) before constructing the reduced subspace. This is because the strain at the surface of the beam is, to leading order, the second spatial derivative of the displacement.

After determining the eigenvalues and eigenvectors \mathbf{q} of \mathbf{A} (Eq. (19a)) in each case, we found the associated POMs via the expansion Eq. (18). Finally, for a given number P of POMs, substituting for $w(x, t)$ in the equation of motion Eq. (1a) using the P -term approximation Eq. (20) yielded, after carrying out the Galerkin

procedure, ROMs consisting of P coupled ODEs in the form of Eq. (21), for each data set.

Subsequently, the accuracy of the ROMs was assessed by estimating the error associated with the displacement and the velocity fields generated by these models. We define the total relative displacement and velocity errors associated with each ROM as

$$\hat{e}_d = \frac{\langle \|w(x, t) - \hat{w}(x, t)\| \rangle}{\langle \|w(x, t)\| \rangle} \quad \text{and} \quad (25a)$$

$$\hat{e}_v = \frac{\langle \|\dot{w}(x, t) - \hat{\dot{w}}(x, t)\| \rangle}{\langle \|\dot{w}(x, t)\| \rangle} \quad (25b)$$

in which the hats indicate values estimated from the ROM, and the time averages are computed over one period.

Figure 2 shows representative results from three different simulations with three different loading conditions, where the model reduction was performed using the displacement field only. Figures 2(a) and 2(b) correspond to non-localized subresonant forcing with low impulsivity (large values of ϵ and τ); Figs. 2(c) and 2(d) also correspond to subresonant forcing, however, with higher impulsivity and higher spatial localization (small values of ϵ and τ); and Figs. 2(e) and

2(f) correspond to a highly impulsive and localized loading condition, but with forcing frequency equal to the second natural frequency of the beam. Examination of the average mechanical energy for each mode, E_N , which is the sum of the modal kinetic and potential energy averaged over one period, reveals that the number of modes excited due to the external forcing is higher in the third case (compare Fig. 2(e) with Figs. 2(a) and 2(c)), so that the effective dimensionality of the response in the third case is higher than the other two cases. Furthermore, the accuracy of the ROM's response is observed to be particularly low in the third case. This can be seen by comparing Fig. 2(f) with Figs. 2(b) and 2(d), where the response corresponding to the mid-point of the beam of the FOS and the ROMs are shown on the (w, \dot{w}) phase plane. In Figs. 2(b) and 2(d), the phase plane plots for the ROM and the FOS overlap almost completely, but not in Fig. 2(f). In fact, the displacement and velocity error estimates (Eqs. (25)) for the third case are quite large, 2.32% and 49.83%, respectively.

We formulated other ROMs for the third case using velocity and strain field data to understand if, with the same mode selection criterion, a different data set would lead to a more accurate ROM. In the left column of Fig. 3, we see that even though the dimensions of these ROMs were larger compared with the displacement-based model (13 POMs were needed for the newer models compared to

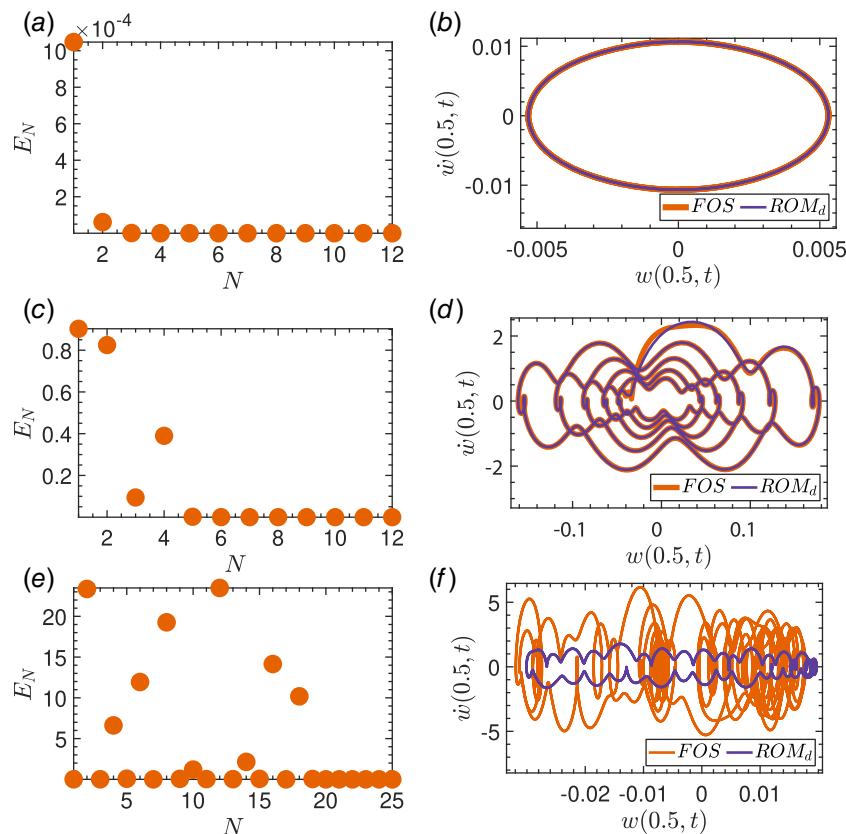


Fig. 2 Reduced order models (ROMs) of driven Euler-Bernoulli beam obtained from displacement field data (ROM_d) with dimension selected using $p = 99.9\%$ of total variance (Eq. (15)). Each row corresponds to a specific loading condition. Left column shows average mechanical energy (E_N) of linear normal modes. Right column compares response of the ROMs with that of full order system (FOS). In panels (a) and (b), forcing is sub-resonant ($T = \pi$) and non-impulsive ($\tau = \pi$, $\epsilon = 2 - \sqrt{2}$; see Eq. (2) and subsequent, and Fig. 1). In panels (c) and (d), forcing is still sub-resonant ($T = \pi$) but is now impulsive ($\tau = 0.001$, $\epsilon = 0.002$). In panels (e) and (f), forcing is at second natural frequency ($T = \frac{1}{2\pi}$) and is impulsive ($\tau = 0.001$, $\epsilon = 0.002$). By visual inspection, we see that the ROM accuracy is quite good in (b), not quite as good in (d), but quite poor in (f). Moreover, we observe that the number of modes excited in the first two cases, (a) and (c), is lower than that in the third case (e). This illustrates that variance-based mode selection does not always yield accurate ROMs, especially under impulsive loading when the effective dimensionality of the response is high.

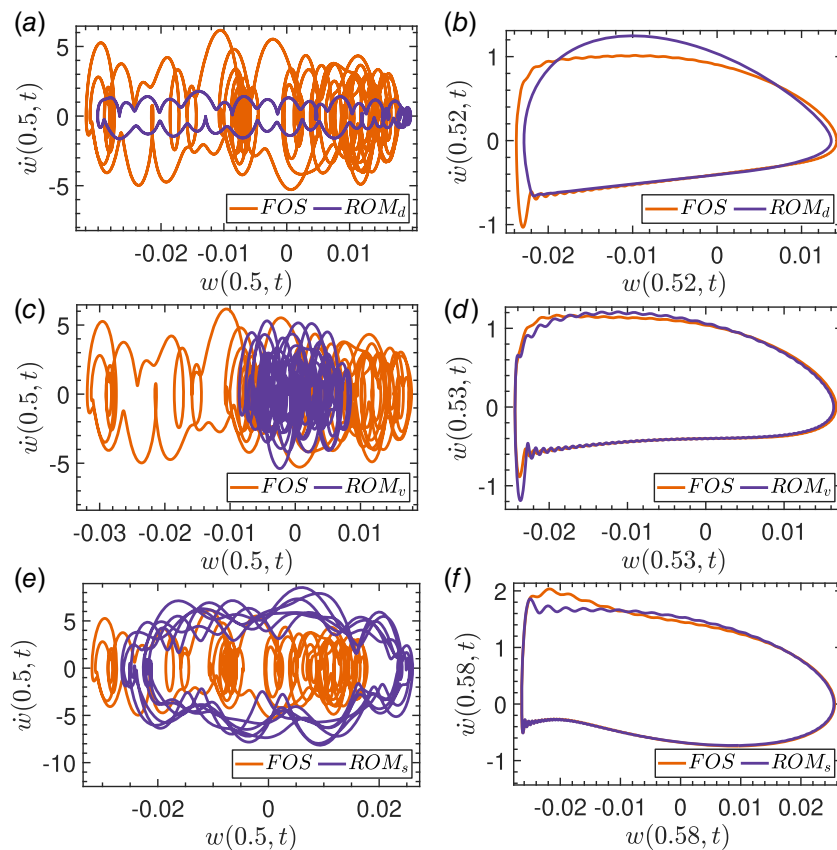


Fig. 3 Accuracy of reduced order models (ROMs) constructed using different data sets, with dimension selected using $p = 99.9\%$ of total variance, as for Fig. 2. In panels (a), (c), and (e): with only viscous damping ($c_v = 1$, $c_m = 0$), displacement versus velocity phase plane plots for the full order system (FOS) and ROMs, based on displacement (ROM_d , $P = 6$ POMs used), velocity (ROM_v , $P = 13$), and strain (ROM_s , $P = 13$) data, respectively. In panels (b), (d), and (f): with only material damping ($c_v = 0$, $c_m = 0.01$), similar plots comparing FOS and ROMs from displacement ($P = 3$), velocity ($P = 5$), and strain ($P = 4$) data, respectively. All remaining parameters match those used for the plots of Figs. 2(e) and 2(f). Each plot is generated at a point on the beam where displacement and velocity errors are high (determined using Eqs. (26)). Note: Fig. 2(f) is duplicated in panel (a) for ease of comparison. See Table 1 for summary of errors for these six cases.

6 for the displacement-based model shown in Fig. 2(e), the accuracy of their response was still not satisfactory. For example, the ROM obtained with strain field data showed 4.52% displacement and 11.87% velocity error. Table 1 summarizes the errors associated with the six ROMs shown in Fig. 3.

In all cases shown in Fig. 3, we observe a clear mismatch between the response of the FOS and the ROMs. Figures in the right column of Fig. 3 correspond to simulations in which the beam was subjected to only material damping, with other parameter values the same as that used to generate the figures on the left,

which were done with viscous damping only. As shown in Table 1, the errors \hat{e}_d and \hat{e}_v are, in general, smaller for the material damping case, likely because with material damping higher vibrational modes are over-damped. Nevertheless, in all cases the ROM errors are substantial, particularly in the velocity.

In the above discussion, we used phase plane plots for specific locations on the beam. To select these locations, we defined the errors

$$e_d(x) = \frac{\left(\left(|w(x, t) - \hat{w}(x, t)|^2 \right)^{\frac{1}{2}} \right)}{\max_t (|w(x, t)|)} \quad \text{and} \quad (26a)$$

$$e_v(x) = \frac{\left(\left(|\dot{w}(x, t) - \hat{\dot{w}}(x, t)|^2 \right)^{\frac{1}{2}} \right)}{\max_t (|\dot{w}(x, t)|)} \quad (26b)$$

in which, as in Eqs. (25), the hats indicate values estimated from the ROM, and the time averages are computed over one period. The quantities $e_d(x)$ and $e_v(x)$ define relative displacement and velocity errors, respectively, as functions of position along the beam. Given that the displacement is zero at the beam's boundaries, these relative errors are not defined at $x = 0$ and $x = 1$; however, our aim was to identify locations in the beam's interior with relatively high errors, so that the ROM inaccuracies would be more

Table 1 Summary of relative errors (Eqs. (25)) associated with reduced order models of Fig. 3, derived using variance-based mode selection

Nature of damping	ROM	\hat{e}_d (%)	\hat{e}_v (%)	P
Viscous	Displacement	2.32	49.83	6
	Velocity	2.48	2.78	13
	Strain	4.52	11.87	13
Material	Displacement	2.57	13.64	3
	Velocity	0.61	2.75	5
	Strain	0.54	5.51	4

Note: P is the number of POMs used in each ROM.

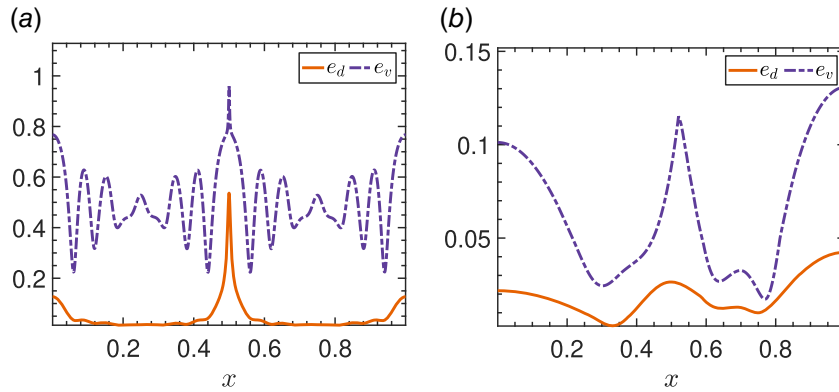


Fig. 4 Relative displacement and velocity errors as a function of position along the beam (Eqs. (26)), for ROMs obtained using displacement field data: (a) only viscous damping (all parameters as in Fig. 3(a)) and (b) only material damping (all parameters as in Fig. 3(b))

readily visible. These errors are shown in Fig. 4 for the ROMs of Figs. 3(a) and 3(b): we see that there is a significant variation in the ROM error over the beam's length, and it is particularly high near the middle. Thus, for the plots in Fig. 3, we chose locations where these errors reached a local maximum, giving $x=0.5$ in Fig. 3(a), $x=0.52$ in Fig. 3(b), etc.

A reduced subspace of dimension P selected using the variance-based mode selection criterion provides an optimal projection of the parent data. Thus, for a given projection error tolerance, it is possible to directly estimate P using Eq. (16). However, the above results demonstrate that the value of P optimal for projecting data does not guarantee a ROM with low modeling error.

To examine the situation in more detail, we denote the projection errors associated with the displacement and the velocity fields as \tilde{e}_d and \tilde{e}_v , respectively. These errors are defined by replacing \hat{w} and $\hat{\dot{w}}$ in Eqs. (25) with the projections \tilde{w} and $\tilde{\dot{w}}$ of the displacement and velocity fields onto the POMs for a given value of P . In Fig. 5, both types of error are plotted against the subspace dimension P : Figs. 5(a) and 5(b) show the projection errors for displacement (\tilde{e}_d) and velocity (\tilde{e}_v), whereas Figs. 5(c) and 5(d) present the corresponding ROM modeling errors (\hat{e}_d and \hat{e}_v).² All plots were generated using only viscous damping as in Figs. 3(a), 3(c), and 3(e). The results show that modeling errors can be very different from projection errors. For example, the decay of the projection errors is generally monotonic with increasing P , but this monotonicity is lost in the ROM errors.

An important feature of the results shown in Fig. 5 is that the maximum subspace dimension is $P=24$ in each case. This upper bound arises from the numerically estimated rank of the associated 100×100 modal correlation matrix A : eigenvectors corresponding to $P > \text{rank}(A)$ define the null space of A and, as a result, are unable to capture the system's dynamics. This suggests that the precision and accuracy of a given data set inherently limits the largest dimension of the data that can be resolved with POD.

The results of Fig. 5 suggest that accurate ROMs may require the number of POMs to exceed the value of P prescribed by variance-based mode selection. Of course, one can always include more POMs by increasing p , the percentage of the data variance captured by the resulting subspace, in a trial and error fashion until a ROM with a desired accuracy is obtained; however that does not explain why $p=99.9\%$ works in some cases, while in other cases 99.99% or 99.999% is required. Moreover, why can this percentage vary substantially not only from system to system but also between different steady-state solutions of the same system? Is it possible to gain

physical insight into the mode selection procedure, beyond this purely statistical analysis?

In the next section, we present an energy-based approach, where P is estimated based on energy balance on the reduced subspace. We show that this approach resolves the ambiguities associated with variance-based dimension estimation.

Mode Selection Based on Energy Closure

As an alternative to variance-based mode selection, we begin by examining the energetics of the system. We observe that because the steady-state dynamics of the system is periodic, the energy dissipated over one period balances the energy input to the system. We can write this as

$$W_d = W_f \quad (27)$$

where

$$W_d = c_v \int_0^T \int_0^1 \dot{w}^2(x, t) dx dt + c_m \int_0^T \int_0^1 \dot{w}'^2(x, t) dx dt \quad (28a)$$

represents the total energy dissipated by the damping forces over one period, and

$$W_f = \int_0^T \int_0^1 f(x; \epsilon, s) g(t; \tau, T) \dot{w}(x, t) dx dt \quad (28b)$$

represents the work input by external forces.

Next, consider the steady-state displacement and velocity fields, $w(x, t)$ and $\dot{w}(x, t)$, of the FOS. We project these exact fields onto a P -dimensional subspace, constructed using POD, to obtain approximations $\tilde{w}(x, t)$ and $\tilde{\dot{w}}(x, t)$. If we now estimate W_d and W_f by substituting the projected approximations into Eqs. (28) for $w(x, t)$ and $\dot{w}(x, t)$, we obtain approximations \tilde{W}_d and \tilde{W}_f . However, for a given value of P , the approximations \tilde{W}_d and \tilde{W}_f will neither be close to their true value W_d (or W_f), nor will they be in balance as in Eq. (27). We, therefore, introduce a residual e_w , defined as

$$e_w = \left| \frac{\tilde{W}_d}{W_d} - \frac{\tilde{W}_f}{W_d} \right| \quad (29)$$

which provides a measure of the energy imbalance on the reduced subspace. Before applying Eq. (29), we require that both \tilde{W}_d/W_d and \tilde{W}_f/W_d be close to 1 to ensure that the energy flowing into and out of the subspace are each being accurately estimated.

²The MATLAB programs used to generate all of the data used in this paper, including the results shown in Figs. 5(c), 5(d), and 6, can be found at <https://doi.org/10.5281/zenodo.4025520>.

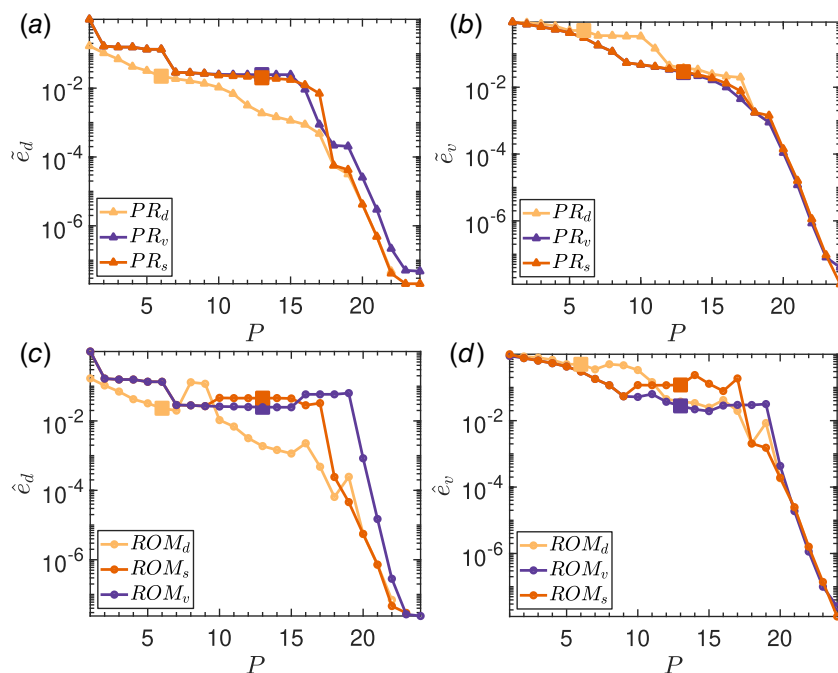


Fig. 5 Comparison between displacement and velocity projection errors (\tilde{e}_d and \tilde{e}_v , top row) and ROM errors (\hat{e}_d and \hat{e}_v , bottom row). Each plot contains separate curves corresponding to system parameters used for Figs. 3(a), 3(c), and 3(e), which included viscous damping only. In panels (a) and (b), the projection errors are plotted against subspace dimension P , computed using displacement (PR_d), velocity (PR_v), and strain (PR_s) data. In panels (c) and (d), modeling errors are similarly plotted against subspace dimension P , for ROMs computed using displacement (ROM_d), velocity (ROM_v), and strain (ROM_s) data. Variance-based mode selection with $p = 99.9\%$ of total variance gives values of P indicated by the large filled square symbols in plots on all four figures. While the projection errors are seen to decrease monotonically with P , that is not the case for the ROM errors.

Then, if $e_w \approx 0$ we can say that the reduced subspace is approximately in energy balance, which suggests that all dynamically relevant dimensions (POMs) have been included.

We thus use e_w , \tilde{W}_d , and \tilde{W}_f to select the correct P for model reduction as an alternative to the variance-based approach. Using the same system parameters as for the plots of Fig. 3, Fig. 6 shows plots of \tilde{W}_d and \tilde{W}_f , normalized by W_d (on the left vertical axis), against the subspace dimension, P . As with the subplots of Fig. 3, Figs. 6(a), 6(c), and 6(e) correspond to the cases with only viscous damping, and Figs. 6(b), 6(d), and 6(f), with only material damping. In every plot, we observe that the normalized \tilde{W}_d and \tilde{W}_f increase monotonically and, beyond a certain value of P , saturate at a value near 1. For example, in Fig. 6(a), \tilde{W}_d and \tilde{W}_f are approximately saturated at $P = 12$, and no noticeable change is observed as P is further increased, indicating that they are very close to their true value, W_d .

However, this does not guarantee that the energy on the subspace is yet in balance. Returning to Fig. 6, we see that in all cases the energy balance error e_w starts at a relatively high value, and then eventually decreases down to a value very close to zero for the maximum value of P . One could simply take this value of P to be the dimension used for the ROM in each case; however, one finds that, while this certainly gives a model of lower dimension than the FOS, it is typically of much higher dimension than is necessary. Furthermore, as discussed in the previous section, the maximum value of P in these plots is determined by the rank of the covariance matrix A (Eqs. (19)) and is a characteristic of the data used for POD. Especially in potential experimental applications, for which the data will invariably be contaminated by noise, this maximum dimension will not be small, but will equal the dimension of the entire data set.

A more systematic approach is to set a tolerance, e_{tol} , indicating an acceptable level of energy balance error and then take the lowest value of P for which $e_w < e_{tol}$ to be the dimension of the ROM. In selecting e_{tol} , one must again ensure that \tilde{W}_f and \tilde{W}_d are estimated accurately since a balance of their inaccurate estimates has no physical significance, but otherwise it can be adjusted to meet the accuracy requirements of the problem at hand, much as one adjusts the tolerance of a differential equation solver or root finder. After some initial experimentation, we found that setting e_{tol} equal to the geometric mean of the minimum and maximum values of e_w (that is, setting $e_{tol} = \sqrt{\max(e_w) \min(e_w)}$) yielded an objective way to select the tolerance that gave consistently accurate ROMs.

However, for the results presented here, we took another approach, which permits us to describe the typical structure of the residual curves. Examining Fig. 6(a), we see that $\tilde{W}_d/W_d \approx \tilde{W}_f/W_d \approx 1$ when $P = 12$, but it is not until $P = 20$ that e_w decreases and then continues to decay with a general downward trend to its minimum value. Hence, we selected $P = 20$ as the dimension of the ROM. This is well beyond the value of $P = 6$ determined using the variance-based approach (refer to the large filled square symbols on the ROM_d curves in Fig. 5). We thus applied a similar procedure to the cases shown in the other subplots of Fig. 6: first, we identified the point at which $\tilde{W}_d/W_d \approx \tilde{W}_f/W_d \approx 1$; then we identified where e_w sharply decreases and continues with a general downward trend to its minimum value. We took the lowest value of P in this trending portion of the residual curve as the dimension of our ROM. This gave us subspace dimensions of $P = 20$ for Fig. 6(c), $P = 18$ for Fig. 6(e), and $P = 8$ for the three cases with material damping, Figs. 6(b), 6(d), and 6(f). Note that the value of P is found to be substantially lower for the systems with material damping. This occurs

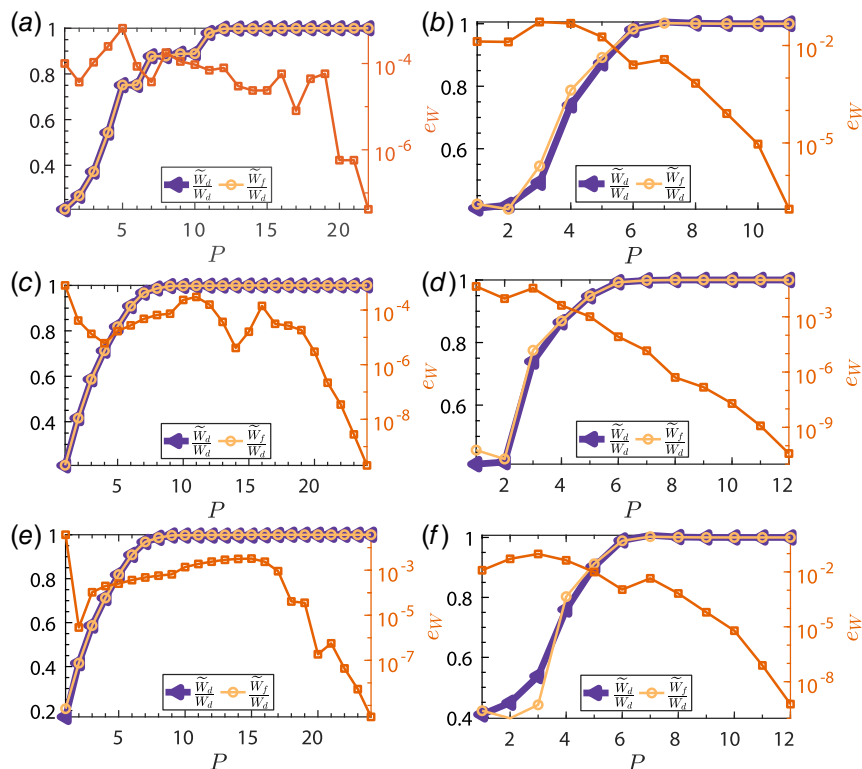


Fig. 6 Energy balance as a function of reduced subspace dimension P . The six subfigures (a)–(f) were computed with the same system parameters used for the corresponding subfigures in Fig. 3. Approximate energy dissipated (\tilde{W}_d) and work input (\tilde{W}_t), calculated by projecting exact displacement and velocity fields onto the reduced subspace, are both normalized by the true dissipated energy W_d (Eq. (28a)) and plotted using the left vertical axis. The energy balance error e_W (Eq. (29)) is plotted using the right axis. Plots (a) and (b) correspond to calculations done with displacement data, (c) and (d) with velocity data, and (e) and (f) with strain data. In each case, the reduced subspace is considered to be energetically closed if $\tilde{W}_d/\tilde{W}_d \approx 1$ and e_W decreases and continues to decay to a small value. The smallest value of P for which this occurs is taken as the number of POMs to be used for the ROM.

because, for material damping, the modal damping coefficient (c_i in Eq. (8)) scales as the square of the natural frequency, so the amplitudes of higher modes are strongly reduced, which diminishes the dimensionality of the system's response. This results in the dynamics of such systems being represented by comparatively lower-dimensional reduced order models.

We reformulated the ROMs using these new values of P and recomputed the displacement and velocity errors, as summarized in Table 2. Comparing Tables 1 and 2, we see that the corresponding displacement and velocity errors of the ROMs obtained using the energy closure criterion are approximately 3 orders of magnitude smaller than those found using the variance-based criterion. This increased accuracy is also evident in Fig. 7, which show steady-state responses of two new ROMs (one with viscous damping, the other with material damping) together with the

exact solutions: the ROM and exact solutions are now virtually indistinguishable. By comparing Fig. 7 to the first row of Fig. 3, the dramatic increase in ROM accuracy is readily apparent. In the interest of brevity, Fig. 7 only displays the results corresponding to ROMs obtained using displacement field data; however, applying the method described above to strain and velocity field data yielded ROMs that show a similar increase in accuracy.

Summary and Conclusions

We have presented a new approach for estimating the dimension of ROMs formulated using POD. We showed that to accurately capture the steady-state dynamics of a high dimensional system

Table 2 Errors associated with different ROMs derived using the energy closure criterion

Nature of damping	ROM	\hat{e}_d (%)	\hat{e}_v (%)	P
Viscous	Displacement	5.53×10^{-4}	1.8×10^{-2}	20
	Velocity	8.39×10^{-2}	4.34×10^{-2}	20
	Strain	2.42×10^{-2}	2.05×10^{-1}	18
Material	Displacement	6.46×10^{-4}	3.67×10^{-2}	8
	Velocity	2.47×10^{-3}	2.51×10^{-3}	8
	Strain	6.47×10^{-4}	3.56×10^{-2}	8

Note: The errors are defined in Eq. (25). P is the number of POMs used in the ROMs.

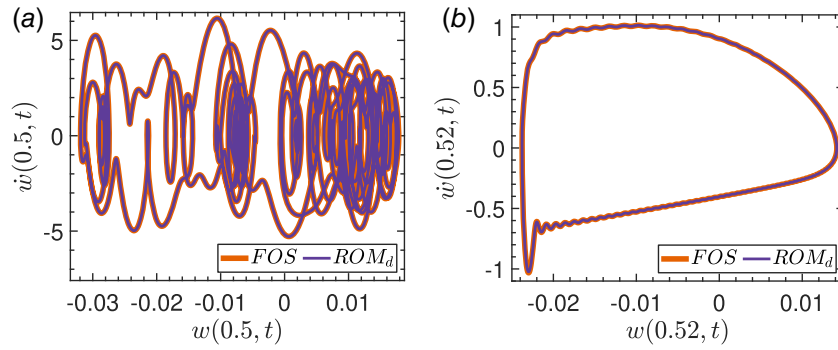


Fig. 7 Phase plane plots comparing responses of FOS and ROM formulated using displacement data, for system with same parameters as in Figs. 3(a) and 3(b). Here, however, the ROM subspace dimension P was chosen using the energy balance criterion. (a) System with viscous damping ($P=20$) and (b) system with material damping ($P=8$). In both cases, the new ROM response is very close to the FOS. ROMs obtained from the other cases in Fig. 3, but using energy closure, show similarly improved accuracy. The ROM errors for all cases are summarized in Table 2. Comparison with Table 1 shows that all errors decreased by about three orders of magnitude.

with a ROM, it is crucial to consider the energy balance on the associated reduced subspace. Our approach uses this idea of *energy closure* to select the number of POMs needed for model reduction. Our findings demonstrate that, while the accuracy of ROMs is influenced by the type of data used to formulate the model, it depends more crucially on the energy balance on the model's reduced subspace.

To focus our discussion, we studied the dynamics of a driven Euler-Bernoulli beam. The beam's distributed periodic forcing could be tuned to excite a variable number of effective degrees-of-freedom. Symbolic algebra was used to obtain approximate analytical steady-state solutions using modal analysis with 100 linear normal modes. These solutions were then used to generate displacement, velocity, and strain data for further processing by POD. Using the conventional variance-based mode selection criterion, which selects POMs that capture a fixed percentage of the total response variance (for our study, 99.9%), yielded ROMs with substantial inaccuracies for more impulsive loading conditions, with a maximum of 4.52% relative displacement error and 49.83% relative velocity error (see Table 1 for details). However, selecting the number of POMs required to achieve energy balance on the corresponding reduced subspace (the span of the selected POMs) gave ROMs with errors that were smaller by approximately three orders of magnitude (Table 2).

A fundamental problem with variance-based mode selection is that it is difficult, a priori, to determine the percentage of total variance that will lead to an accurate model. Furthermore, the needed percentage of variance can differ widely from one system to the next, or even from one steady-state solution to another. There are two main reasons for this. First, POD is essentially a projection-based technique that ensures optimal reduction (in a mean-square statistical sense) of high-dimensional data. However, such projection optimality does not ensure accuracy of a ROM. This is because, second, the variance of a data set, or any portion of it in a reduced subspace, has no direct connection with the dynamics of the system generating it. In particular, dynamically important modes that have small variance can still play a crucial role in transporting energy in and out of the system. The neglect of such small-variance degrees-of-freedom can result in a ROM with behavior that significantly deviates from the true system dynamics.

The energy closure criterion resolves this problem by directly examining whether the subspace spanned by a candidate set of POMs is closed with respect to the energy flowing into and out of it. Thus, instead of merely assessing the relative magnitude of different POMs, energy closure analysis gives a physics-based explanation for why selected modes should be included in a ROM.

It provides a physically grounded and objective criterion for mode selection that can be used across systems and steady-states, obviating the need for ad hoc changes in the percentage of captured variance, as can occur with the conventional, purely statistical approach.

For conceptual clarity and numerical convenience, this paper focused on the dynamics of a relatively simple Euler-Bernoulli beam. The general application of the energy closure criterion will require that certain practical issues surrounding its implementation be addressed. For the study of experimental systems or finite element models, the semi-analytical approach employed here can not be used, simply because a closed-form solution for the dynamics will typically not be available. This will be especially true for non-linear systems. However, the physical principle underlying energy closure has universal validity; hence, there is no fundamental reason to think the approach could not, in principle, be applied in such cases. What is needed is a numerical implementation of the ideas developed in this paper. Moreover, energy closure analysis requires the velocity field of the system, which for experimental systems may be difficult to acquire directly. One may be able to use finite differences or interpolation methods to estimate the velocity field in such cases. The effect of such approximations, as well as the effect of experimental noise and measurement error, on dimension estimates made using the energy closure criterion will have to be studied in future work.

Conflict of Interest

There are no conflicts of interest.

Data Availability Statement

The datasets generated and supporting the findings of this article are obtainable from the corresponding author upon reasonable request. The authors attest that all data for this study are included in the paper.

References

- [1] Sirovich, L., 1987, "Turbulence and the Dynamics of Coherent Structures Part I: Coherent Structures," *Quart. Appl. Math.*, **45**(3), pp. 561–571.
- [2] Sirovich, L., 1989, "Chaotic Dynamics of Coherent Structures," *Physica D: Nonlinear Phenomena*, **37**(1), pp. 126–145.
- [3] Holmes, P., Berkooz, G., and Lumley, J. L., 1996, *Turbulence, Coherent Structures, Dynamical Systems and Symmetry*, Cambridge University Press, Cambridge, UK.

- [4] Bergmann, M., 2017, "A Hybrid DNS/ROM Approach for Wind and Ocean Wave Energy Converters," MECASIF Workshop 2017—MECASIF on Reduced Order Methods for Wind and Marine Current Power, Sophia Antipolis, France.
- [5] Kammerer, A. J., and Hackett, E. E., 2017, "Use of Proper Orthogonal Decomposition for Extraction of Ocean Surface Wave Fields From X-band Radar Measurements of the Sea Surface," *Remote Sens.*, **9**(9), p. 881.
- [6] Solari, G., Carassale, L., and Tubino, F., 2007, "Proper Orthogonal Decomposition in Wind Engineering. Part 1: A State-of-the-Art and Some Prospects," *Wind Struct.*, **10**(2), pp. 153–176.
- [7] Carassale, L., Solari, G., and Tubino, F., 2007, "Proper Orthogonal Decomposition in Wind Engineering. Part 2: Theoretical Aspects and Some Applications," *Wind Struct.*, **10**(2), pp. 177–208.
- [8] Aa, E., Ridley, A., Huang, W., Zou, S., Liu, S., Coster, A. J., and Zhang, S., 2018, "An Ionosphere Specification Technique Based on Data Ingestion Algorithm and Empirical Orthogonal Function Analysis Method," *Space Weather*, **16**(9), pp. 1410–1423.
- [9] Tatli, H., and Türkeş, M., 2011, "Empirical Orthogonal Function Analysis of the Palmer Drought Indices," *Agric. For. Meteorol.*, **151**(7), pp. 981–991.
- [10] Ravindran, S. S., 2000, "A Reduced-Order Approach for Optimal Control of Fluids Using Proper Orthogonal Decomposition," *Int. J. Numerical Methods Fluids*, **34**(5), pp. 425–448.
- [11] Kunisch, K., and Volkwein, S., 2008, "Proper Orthogonal Decomposition for Optimality Systems," *ESAIM: Math. Model. Numer. Anal. Modélisation Math. Anal. Numér.*, **42**(1), pp. 1–23.
- [12] El Moçayd, N., Mohamed, M. S., Ouazar, D., and Seaid, M., 2020, "Stochastic Model Reduction for Polynomial Chaos Expansion of Acoustic Waves Using Proper Orthogonal Decomposition," *Reliab. Engin. Syst. Safety*, **195**, Article No. 106733.
- [13] Balasubramanian, M., Zabic, S., Bowd, C., Thompson, H. W., Wolenski, P., Iyengar, S. S., Karki, B. B., and Zangwill, L. M., 2009, "A Framework for Detecting Glaucomatous Progression in the Optic Nerve Head of An Eye Using Proper Orthogonal Decomposition," *IEEE Trans. Inform. Technol. Biomed.*, **13**(5), pp. 781–793.
- [14] Kellem, A. R., Chaturantabut, S., Sorensen, D. C., and Cox, S. J., 2010, "Morphologically Accurate Reduced Order Modeling of Spiking Neurons," *J. Comput. Neurosci.*, **28**(3), pp. 477–494.
- [15] Ting, Z., and Hui, J., 2012, "EEG Signal Processing Based on Proper Orthogonal Decomposition," 2012 International Conference on Audio, Language and Image Processing, Shanghai, China, July 16–18, IEEE.
- [16] Shlizerman, E., Ding, E., Williams, M. O., and Kutz, J. N., 2012, "The Proper Orthogonal Decomposition for Dimensionality Reduction in Mode-Locked Lasers and Optical Systems," *Int. J. Optics*, **2012**, pp. 1–18.
- [17] Cusumano, J. P., and Bai, B. Y., 1993, "Period-infinity Periodic Motions, Chaos, and Spatial Coherence in a 10 deg of Freedom Impact Oscillator," *Chaos, Solitons Fractals*, **3**(5), pp. 515–535.
- [18] Cusumano, J. P., Sharkady, M. T., and Kimble, B. W., 1994, "Experimental Measurements of Dimensionality and Spatial Coherence in the Dynamics of a Flexible-Beam Impact Oscillator," *Philos. Trans. Phys. Sci. Engin.*, **347**(1683), pp. 421–438.
- [19] Han, S., and Feeny, B., 2003, "Application of Proper Orthogonal Decomposition to Structural Vibration Analysis," *Mech. Syst. Signal Process.*, **17**(5), pp. 989–1001.
- [20] Feeny, B. F., and Kappagantur, R., 1998, "On the Physical Interpretation of Proper Orthogonal Modes in Vibrations," *J. Sound. Vib.*, **211**(4), pp. 607–616.
- [21] Kappagantur, R., and Feeny, B. F., 1999, "An 'optimal' Modal Reduction of a System with Frictional Excitation," *J. Sound. Vib.*, **224**(5), pp. 863–877.
- [22] Azeez, M., and Vakakis, A., 2001, "Proper Orthogonal Decomposition (POD) of a Class of Vibroimpact Oscillations," *J. Sound. Vib.*, **240**(5), pp. 859–889.
- [23] Wolter, C., Trindade, M., and Sampaio, R., 2002, "Reduced-Order Model for An Impacting Beam Using the Karhunen-Loève Expansion," *TEMA - Tendências em Matemática Aplicada e Computacional*, **3**(2).
- [24] Amabili, M., Sarkar, A., and Paidoussis, M., 2006, "Chaotic Vibrations of Circular Cylindrical Shells: Galerkin Versus Reduced-Order Models Via the Proper Orthogonal Decomposition Method," *J. Sound. Vib.*, **290**(3–5), pp. 736–762.
- [25] Amabili, M., and Touzé, C., 2007, "Reduced-order Models for Nonlinear Vibrations of Fluid-filled Circular Cylindrical Shells: Comparison of POD and Asymptotic Nonlinear Normal Modes Methods," *J. Fluids Struct.*, **23**(6), pp. 885–903.
- [26] Ritto, T. G., Buezas, F. S., and Sampaio, R., 2012, "Proper Orthogonal Decomposition for Model Reduction of a Vibroimpact System," *J. Brazilian Soc. Mech. Sci. Engin.*, **34**(3), pp. 330–340.
- [27] Eftekhar Azam, S., and Mariani, S., 2013, "Investigation of Computational and Accuracy Issues in POD-based Reduced Order Modeling of Dynamic Structural Systems," *Engin. Struct.*, **54**, pp. 150–167.
- [28] Kreuzer, E., and Kust, O., 1996, "Analysis of Long Torsional Strings by Proper Orthogonal Decomposition," *Archive Appl. Mech.*, **67**(1), pp. 68–80.
- [29] Georgiou, I. T., and Schwartz, I. B., 1999, "Dynamics of Large Scale Coupled Structural/Mechanical Systems: A Singular Perturbation/proper Orthogonal Decomposition Approach," *SIAM J. Appl. Math.*, **59**(4), pp. 1178–1207.
- [30] Kerschen, G., 2002, "On the Model Validation in Nonlinear Structural Dynamics," PhD dissertation, Université de Liège, Liège, Belgium.
- [31] Segala, D. B., and Naseradinmousavi, P., 2017, "On the Inclusion of Time Derivatives of State Variables for Parametric Model Order Reduction for a Beam on a Nonlinear Foundation," *ASME J. Dyn. Syst. Meas. Control.*, **139**(8), p. 081009.
- [32] Rathinam, M., and Peltzold, L. R., 2003, "A New Look At Proper Orthogonal Decomposition," *SIAM J. Numer. Anal. Philadelphia*, **41**(5), pp. 1893–1925.
- [33] Ilbeigi, S., and Chelidze, D., 2017, "Persistent Model Order Reduction for Complex Dynamical Systems Using Smooth Orthogonal Decomposition," *Mech. Syst. Signal Process.*, **96**, pp. 125–138.
- [34] Segala, D. B., and Chelidze, D., 2014, "Robust and Dynamically Consistent Model Order Reduction for Nonlinear Dynamic Systems," *ASME J. Dyn. Syst. Meas. Control.*, **137**(2), p. 021011.
- [35] Chelidze, D., 2014, "Identifying Robust Subspaces for Dynamically Consistent Reduced-Order Models," In Kerschen G. (ed.) *Nonlinear Dynamics*, Volume 2. Conference Proceedings of the Society for Experimental Mechanics Series, Springer, Cham.
- [36] Ilbeigi, S., and Chelidze, D., 2018, "A New Approach to Model Reduction of Nonlinear Control Systems Using Smooth Orthogonal Decomposition," *Int. J. Robust Nonlinear Control*, **28**(15), pp. 4367–4381.
- [37] Guo, X., and Przekop, A., 2010, "Energy-based Modal Basis Selection Procedure for Reduced-order Nonlinear Simulation," 51st AIAA/ASME/ASCE/AHS/ASC Structures, Structural Dynamics, and Materials Conference, Orlando, FL, Apr. 12–15, AIAA.
- [38] Bhattacharyya, S., and Cusumano, J. P., 2019, "The Importance of Energy Criteria for Selecting Modes in Reduced Order Modeling," ASME 2019 International Design Engineering Technical Conferences and Computers and Information in Engineering Conference, Anaheim, CA, Aug. 18–21, ASME.
- [39] Meirovitch, L., 2001, *Fundamentals of Vibrations*, McGraw-Hill, New York.
- [40] Fernandez, T. N., 2010, "Analytical Computation of Proper Orthogonal Decomposition Modes and n-width Approximations for the Heat Equation with Boundary Control," Master's thesis, University of Tennessee, Knoxville, TN.
- [41] Liang, Y., Lee, H., Lim, S., Lin, W., Lee, K., and Wu, C., 2002, "Proper Orthogonal Decomposition and Its Applications—Part I: Theory," *J. Sound. Vib.*, **252**(3), pp. 527–544.
- [42] Liang, Y., Lin, W., Lee, H., Lim, S., Lee, K., and Sun, H., 2002, "Proper Orthogonal Decomposition and Its Applications—part II: Model Reduction for MEMS Dynamical Analysis," *J. Sound. Vib.*, **256**(3), pp. 515–532.
- [43] Djouadi, S. M., 2008, "On the Optimality of the Proper Orthogonal Decomposition and Balanced Truncation," 2008 47th IEEE Conference on Decision and Control, Cancun, Mexico, Dec. 9–11, IEEE.